

A Large-Eddy Simulation Study of Bottom-Heating Effects on Scalar Dispersion in and above a Cubical Building Array

SEUNG-BU PARK, JONG-JIN BAIK, AND YOUNG-HEE RYU

School of Earth and Environmental Sciences, Seoul National University, Seoul, South Korea

(Manuscript received 18 September 2012, in final form 18 January 2013)

ABSTRACT

Thermal effects on scalar dispersion in and above a cubical building array are numerically investigated using the parallelized large-eddy simulation model (PALM). Two cases (no heating and bottom heating) are simulated, and scalar dispersion patterns in the two cases are compared. In the no-heating case, scalar ejections in the low-speed flow structures play an important role in transporting scalar upward above the building array. In the bottom-heating case, streamwise elongated and isolated scalar ejections appear below upper low-speed and upper high-speed regions above the building array. In both cases, bottom-emitted scalar flux is balanced by streamwise scalar advection and vertical turbulent scalar flux at the rooftop height. The vertical turbulent scalar flux at the rooftop height is mainly composed of scalar ejections and scalar sweeps that are related to low- and high-speed flow structures, respectively. Furthermore, the low- and high-speed flow structures at the rooftop height induce spanwise converging and spanwise diverging flow in the building array in both the no-heating and bottom-heating cases. Thus, the mean scalar concentration in the building array is high below the low-speed flow structures (above the building array) in both cases. Dominant scalar dispersion patterns in the building array are found to be spanwise scalar transport events that are composed of negative scalar concentration perturbation and spanwise flow therein. In the bottom-heating case, a large-scale secondary circular flow develops, causing stronger spanwise scalar dispersion patterns in the building array.

1. Introduction

Building-scale or street canyon-scale scalar dispersion in urban areas is one of the important issues in urban boundary layer meteorology because of its impacts on air quality and human health as well as being of fluid-dynamical interest. Despite its significant influence on daily life, however, the small-scale scalar dispersion phenomenon, as exemplified by dispersion of vehicle-emitted pollutants in a street canyon, is still not well understood. In contrast with rural areas, various building geometries and urban surface heating induce turbulent flow and dispersion in urban areas, making it more difficult to understand scalar dispersion therein. Scalar dispersion in and above idealized street canyons has been extensively studied through wind-tunnel experiments, field observations, and numerical simulations (Davidson

et al. 1995; Meroney et al. 1996; Sini et al. 1996; Macdonald et al. 1997; Kim and Baik 2004). These studies have focused on the mean and statistical features of scalar dispersion in urban areas and not on its instantaneous features.

Despite the importance of the turbulent processes to scalar dispersion in urban areas, our understanding of turbulent scalar dispersion has progressed slowly because of an insufficient understanding of unsteady flow in urban areas. Walton and Cheng (2002) conducted a large-eddy simulation (LES) of scalar dispersion in an idealized street canyon and illustrated pollutant removal processes from the street canyon that occur periodically on a 30–60-s time scale. They emphasized the unsteady and intermittent features of the pollutant removal processes. Kanda et al. (2004) conducted LES of turbulent flow over building arrays and showed that turbulence coherent structures such as low-speed streaks and streamwise vortices appear above the building array. Coceal et al. (2007) suggested a conceptual model that relates turbulence coherent structures to the vertical transport of momentum. They suspect that the vertical

Corresponding author address: Jong-Jin Baik, School of Earth and Environmental Sciences, Seoul National University, Seoul 151-742, South Korea.
E-mail: jjbaik@snu.ac.kr

transport of scalar is closely related to the turbulence coherent structures such as low-speed streaks. Takimoto et al. (2011) also emphasized the correlation of the flushing of tracer particles from the canopy layer and the low-speed regions passing above the canopy on the basis of particle image velocimetry measurements. Michioka et al. (2011) recently simulated scalar removal from a two-dimensional street canyon using an LES model. They classified pollutant removal into several patterns and investigated the relationship between the patterns and turbulence coherent structures (low-speed streaks) above the street canyon.

Urban surface heating can significantly affect scalar dispersion patterns in urban areas by inducing different turbulence coherent structures or just by increasing the activity of turbulent eddies. Previous studies have focused on the mean and statistical features of thermally affected scalar dispersion in urban areas, however (Kim and Baik 1999; Uehara et al. 2000; Louka et al. 2002). Thus, it is necessary to investigate thermal effects on time-varying flow structures and scalar fields in urban areas to better understand the instantaneous features of scalar dispersion in variable thermal environments.

In this study, we investigate scalar dispersion in and above a building array in neutrally and unstably stratified environments, focusing on thermal effects on characteristic scalar dispersion patterns. The LES model and simulation setup are described in section 2. In section 3, the LES model is validated using wind-tunnel experimental data. In section 4, simulation results are presented and discussed. A summary and conclusions are given in section 5.

2. Model description and simulation setup

In this study, the parallelized LES model (PALM) developed at the Leibniz University of Hannover, Germany (Raasch and Schröter 2001; Letzel et al. 2008), is used to simulate scalar dispersion in and above a cubical building array. The governing equations in PALM are implicitly filtered Boussinesq equations. The momentum equation, thermodynamic energy equation, subgrid-scale (SGS) turbulent kinetic energy (TKE) equation, and passive scalar (pollutant) equation are numerically solved using the third-order Runge–Kutta scheme for time integration and the second-order Piacsek and Williams (1970) scheme for advection. The SGS turbulent fluxes are parameterized using the 1.5-order Deardorff (1980) scheme that uses SGS TKE to calculate eddy viscosity. Except for the addition of the passive scalar equation, the simulation setup in this study is the same as that of Park and Baik (2013). The detailed analysis results of turbulence coherent structures are given in that paper.

Figure 1a shows the computational domain and building configuration. The computational domain size is 480 m in the x (streamwise) direction, 480 m in the y (spanwise) direction, and 550 m in the z (vertical) direction. The grid size in both the x and y directions is 1 m. The grid size in the z direction is uniform with 1 m up to $z = 100$ m and then gradually increases with an expansion ratio of 1.08. A cubical building array is considered, and 20-m-height cubical buildings are arranged in lines with a constant spacing of 20 m in both the x and y directions. The plan area density of the building array is 25%, and the aspect ratio of the street canyon is 1. Thus, a skimming flow regime is expected to occur in the building array (Macdonald et al. 1997).

The cyclic boundary condition is applied at the lateral boundaries for velocity components, temperature, and SGS TKE. For passive scalar, the cyclic boundary condition is applied at the spanwise boundaries and the Dirichlet and radiation boundary conditions are applied at the inflow and outflow boundaries, respectively. The passive scalar concentration is set equal to 0 at the inflow boundary to maintain a quasi-steady mean state of scalar. The zero-gradient boundary condition is applied for all of the variables at the top boundary. The initial ambient wind blows in the x direction, and its vertical profile is logarithmic with a friction velocity of 0.43 m s^{-1} . Flow in the computational domain is maintained by applying a constant external pressure gradient (-0.001 Pa m^{-1}) in the x direction, and the Coriolis effect is not included in this study. At the grid points closest to all solid surfaces, Monin–Obukhov similarity is employed in the momentum equation and thermodynamic energy equation. In consideration that pollutants are continuously emitted from all of the streets, the passive scalar flux at all grid points of the bottom is set to $5 \mu\text{g m}^{-2} \text{ s}^{-1}$.

The no-heating (NH) case and street bottom–heating (BH) case are simulated to investigate thermal effects on scalar dispersion. The temperature of the street bottom is set to be higher than that of the ambient air by 10 K, and the bulk Richardson number in the BH case is -0.31 . PALM is integrated for 4.5 h in the NH case, and the last 30 min of simulation data are used for analysis unless otherwise mentioned. Then, PALM is integrated for one more hour with the street bottom being heated, and the last 30 min of simulation data of the BH case are analyzed.

3. Validation

The LES model is validated using the wind-tunnel data from the Compilation of Experimental Data for Validation of Microscale Dispersion Models (CEDVAL) database hosted at the University of Hamburg (online at

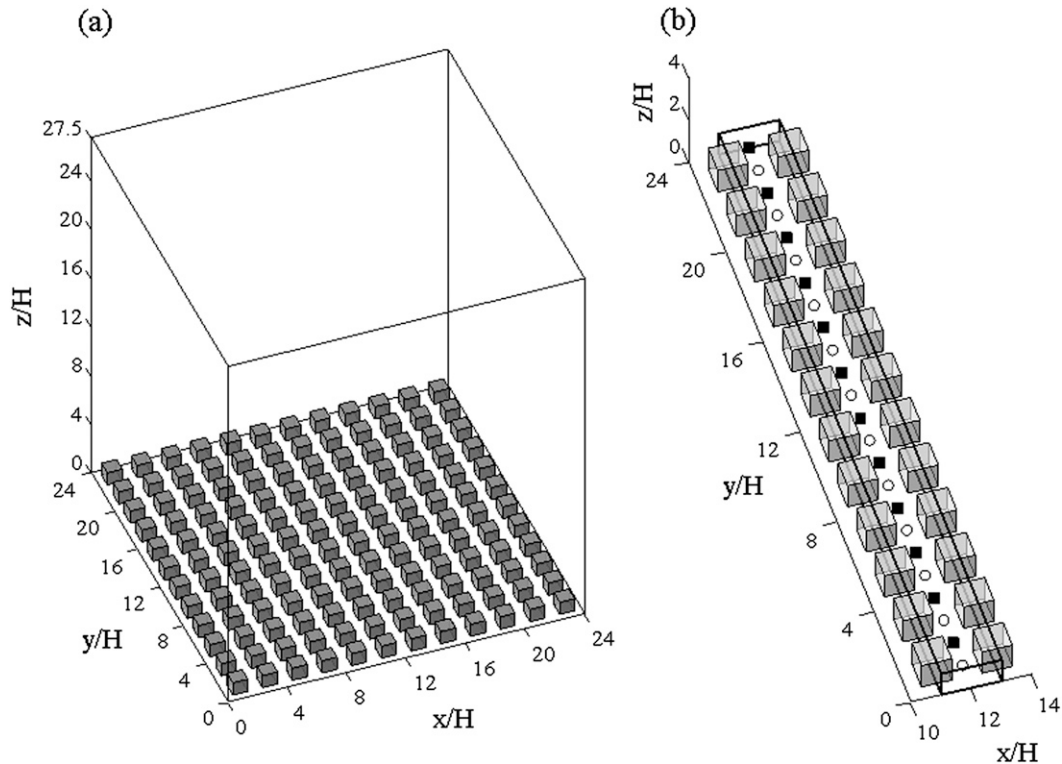


FIG. 1. Illustrations of (a) the computational domain and building configuration (after Park and Baik 2013) and (b) the sampling points of the vertical profiles shown later in Fig. 3. Here, H is the building height.

<http://www.mi.uni-hamburg.de/cedval.html>). For this, a numerical simulation with a 3×7 rectangular building array is conducted and the normalized scalar concentration field around the scalar sources (including the cavity spaces between the fifth and sixth buildings) is compared with that of the wind-tunnel experiment. Figure 2 shows the normalized mean scalar concentration fields at $z/H = 0.06$ in the wind-tunnel experiment and numerical simulation. The normalized mean scalar concentration in the numerical simulation is defined as $K = U_{\text{ref}} H^2 C_m / [A(\bar{c}'w')_0]$, where U_{ref} is the mean streamwise velocity magnitude at $z/H = 1$, H is the building height, C_m is the measured mean scalar concentration, A is the area of scalar sources, and $(\bar{c}'w')_0$ is the vertical scalar flux at the bottom ($5 \mu\text{g m}^{-2} \text{s}^{-1}$). The ratio of block height in the wind-tunnel experiment and building height in the numerical simulation is 1:200, and the scales in the x and y directions in Fig. 2 are normalized by the block height or building height. In the wind-tunnel experiment and numerical simulation, the overall magnitudes of normalized mean scalar concentration are similar to each other. Although there are some discrepancies of mean scalar fields in the central region of cavity space that are due to strongly simulated double-eddy circulation there, overall the mean scalar distribution patterns are similar to each other.

4. Results and discussion

a. Vertical turbulent scalar flux

Figure 3 shows the vertical profiles of the 12-point-averaged mean scalar concentration \bar{c} , vertical turbulent scalar flux $\bar{c}'w'$, standard deviation of vertical velocity (or root-mean-square of vertical velocity perturbation) $(\bar{w}'^2)^{1/2}$, and ratio of scalar sweep to scalar ejection. Variables c' and w' denote deviations from the time-averaged scalar concentration \bar{c} and vertical velocity \bar{w} , respectively. SGS parts are excluded in the calculated turbulence statistics because their magnitudes are much smaller than the magnitudes of resolved parts. The space ($11.5 \leq x/H \leq 12.5$, $0 \leq y/H \leq 24$, $0 \leq z/H \leq 1$) is divided into cavity and intersection spaces, and the vertical profiles that are averaged over the 12 cavity center (CC) points and those that are averaged over the 12 intersection center (IC) points (Fig. 1b) are compared in the NH and BH cases.

Over the IC points, the mean scalar concentration decreases monotonically with height in both the NH and BH cases (Fig. 3a), indicating that the scalar transport process over the IC points is similar to that over a flat surface. On the contrary, the mean scalar concentration abruptly decreases with height above an inflection point at $z/H \sim 1$ over the CC points in both cases. Over the CC

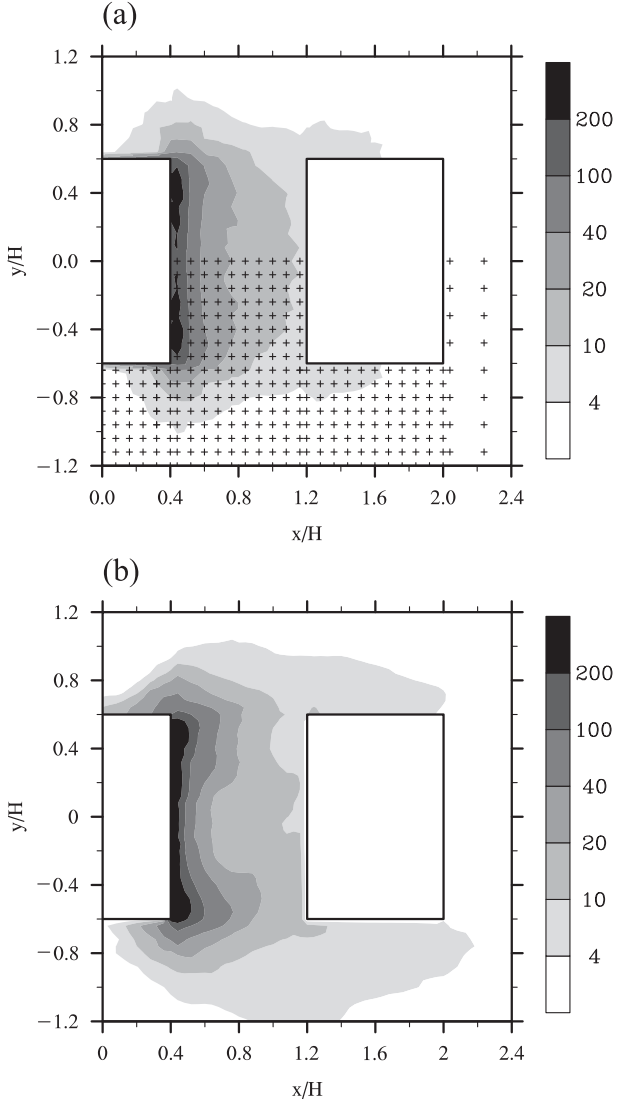


FIG. 2. Normalized mean scalar concentration fields at $z/H = 0.06$ in (a) the wind-tunnel experiment and (b) the numerical simulation presented in this paper.

points, the mean scalar concentration within the canopy is higher than that over the IC points in both cases because plenty of scalars emitted from the bottom are trapped following the mean vortex flow (a canyon vortex in the x - z plane and a double-eddy circulation in the x - y plane) in the cavity spaces. Canyon vortices in the cavity spaces increase scalar concentration, especially in the leeward upper part of cavity spaces, leading to active upward scalar transport. Over both the CC and IC points, the mean scalar concentration is lower in the BH case than in the NH case because more scalars are transported upward following thermally induced vertical turbulent motions in the BH case. Actual magnitude of vertical turbulent scalar flux at the rooftop height in

the BH case is slightly larger than that in the NH case over both the CC and IC points (Fig. 3b), however, because the standard deviation of vertical velocity in the BH case is larger than that in the NH case (Fig. 3c). Bottom heating induces stronger vertical turbulent scalar flux at the rooftop height without any noticeable change in mean vortex flow in cavity spaces (not shown). Over the CC points, in both the NH and BH cases, the vertical turbulent scalar flux has local peaks at the rooftop height (due to a large vertical gradient of scalar concentration) and at the lower part. Over the IC points, the vertical turbulent scalar flux has its maximum at $z/H \sim 0.6$ in the NH case and at $z/H \sim 1$ in the BH case.

Over both the CC and IC points, $(\overline{w'^2})^{1/2}$ tends to increase up to the rooftop height with its magnitude being larger in the BH case than in the NH case (Fig. 3c). While $(\overline{w'^2})^{1/2}$ decreases with height above $z/H \sim 1.9$ (2.2) in the NH case, $(\overline{w'^2})^{1/2}$ in the BH case decreases with height above $z/H \sim 1.4$ (0.9) and increases again with height above $z/H \sim 3.5$ (3.7) over the CC points (IC points), reaching its maximum at $z/H \sim 15$ (a little higher than half the domain height). This implies that large-scale vertical motions exist in the BH case as in the buoyancy-driven planetary boundary layer (Moeng and Sullivan 1994).

As in the quadrant analysis of vertical turbulent momentum flux, the instantaneous vertical turbulent scalar flux $c'w'$ at one position can be classified into four quadrants: scalar ejection ($c'_+ w'_+$), scalar outward interaction ($c'_- w'_+$), scalar sweep ($c'_- w'_-$), and scalar inward interaction ($c'_+ w'_-$) (Katul et al. 1997). If a scalar source exists below the reference point, turbulent motions transport scalar upward by inducing scalar ejections and scalar sweeps and the ratio of the two events is sensitive to the type of turbulent flow. The vertical profiles of the scalar sweep:ejection ratio are plotted in Fig. 3d. Except for local peaks at the rooftop height, the ratio tends to decrease with height from the value larger than one near the bottom to the value less than one above the rooftop height in both the NH and BH cases. This indicates that turbulent motions transport scalar upward mostly by inducing scalar sweeps below the rooftop height and mostly by inducing scalar ejections above the rooftop height. The local peaks of the ratio at the rooftop height over the CC points indicate the dominance of scalar sweeps at the tops of cavity spaces in both the NH and BH cases.

Figure 4 shows multiresolution cospectra of c and w (or multiresolution decomposed scalar fluxes) at four heights ($z/H = 3, 1.2, 1$, and 0.5) over the CC and IC points in the NH and BH cases. The last 2048 s of simulation data are used to calculate the multiresolution cospectra in both cases. Multiresolution cospectra are

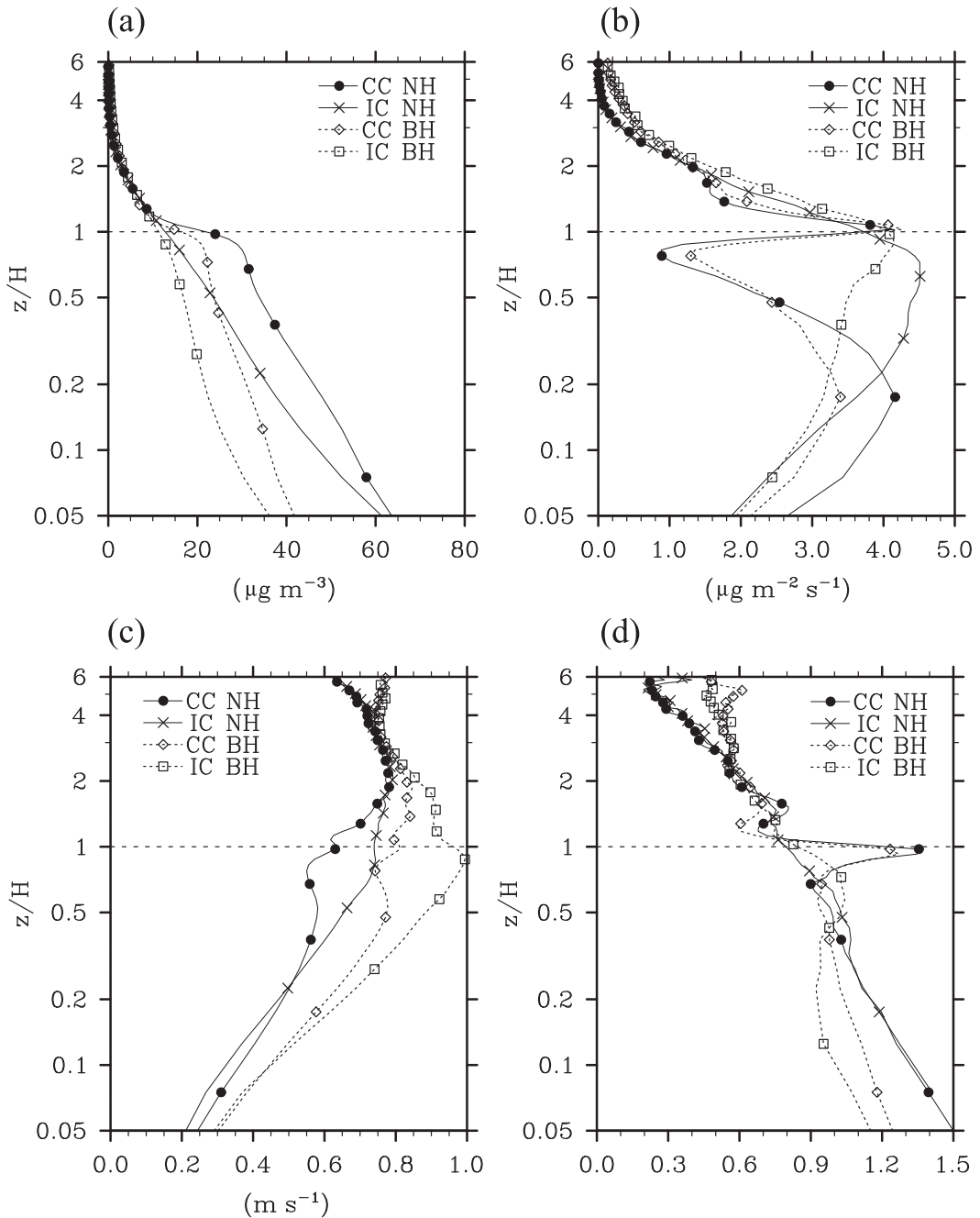


FIG. 3. Vertical profiles of 12-point-averaged (a) mean scalar concentration, (b) vertical turbulent scalar flux, (c) standard deviation of vertical velocity [based on Park and Baik (2013)], and (d) ratio of scalar sweep to scalar ejection in the NH and BH cases. In Fig. 1b, the sampling points of these vertical profiles are marked as open circles for cavity centers (CC) and as filled squares for intersection centers (IC). Note that the vertical axis (z/H) is on a logarithmic scale.

constructed by orthogonally decomposing the vertical turbulent scalar flux into components having various averaging widths (Mahrt and Gibson 1992). The multi-resolution flux decomposition method is very similar to the Fourier spectrum analysis. By using the multi-resolution flux decomposition method, the components

of vertical turbulent scalar flux can be calculated and their magnitudes can be directly compared with each other (Howell and Mahrt 1997).

At $z/H = 3$ (far above the rooftop height), the co-spectra have maxima at averaging widths of 8 or 16 s in all cases. The magnitude of cospectra in the BH case is

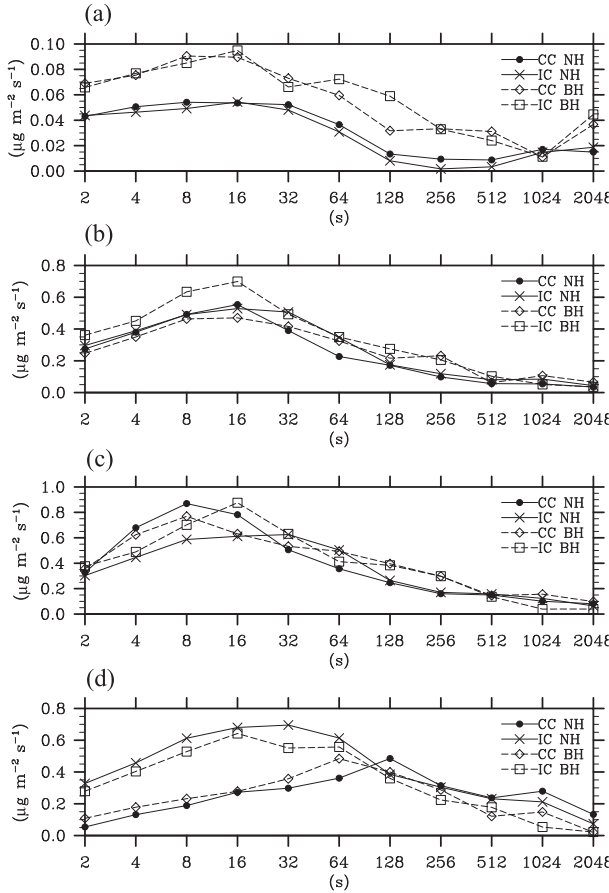


FIG. 4. Multiresolution cospectra of c and w at z/H = (a) 3, (b) 1.2, (c) 1, and (d) 0.5 over the CC and IC points in the NH and BH cases.

larger than that in the NH case except for an averaging width of 1024 s. The difference in the cospectra magnitude is attributed to more active scalar ejection events in the BH case than in the NH case. The difference becomes smaller with decreasing height down to $z/H = 1.2$ (Fig. 4b). At $z/H = 1.2$, the cospectra have maxima at an averaging width of 16 s in all cases. Especially below $z/H = 1.2$, the distribution of cospectra over the IC points does not change much with height, indicating that a similar transport process dominates scalar transport even in the building canopy layer. On the other hand, maxima of cospectra at a shorter averaging width (8 s) appear over the CC points at the rooftop height in both the NH and BH cases. As shown in Fig. 3d, scalar sweeps dominate scalar upward transport at the rooftop height over the CC points. Thus, the cospectra maximum at the shorter averaging width might be due to the dominance of scalar sweeps that are generated or strengthened by shear instability at the tops of cavity spaces. At $z/H = 0.5$, over the CC points, the cospectra have maxima at

longer averaging widths (128 s in the NH case and 64 s in the BH case) because of the absence of dominant scalar sweeps at that height.

b. Scalar dispersion above a building array

To investigate characteristic scalar dispersion patterns and their relationship with turbulence coherent structures (e.g., low-speed streaks), the fields of $\text{sgn}(w') \times \max(0, c'w')$ with the contours of equal streamwise velocity (5.5 m s^{-1}) at $t = 15\,480$ s in the NH case and those at $t = 19\,080$ s in the BH case are shown in Fig. 5. The fields of $\text{sgn}(w') \times \max(0, c'w')$ instead of $c'w'$ are plotted to emphasize scalar ejections and scalar sweeps (Park et al. 2012). The $\max(0, c'w')$ returns the magnitude of $c'w'$ only when $c'w'$ is positive (when scalar is transported upward), and $\text{sgn}(w')$ returns the sign of vertical velocity perturbation. Therefore, a positive value of $\text{sgn}(w') \times \max(0, c'w')$ indicates a scalar ejection event (a combination of positive c' and positive w') and a negative value indicates a scalar sweep event (a combination of negative c' and negative w') following a typical definition used in the quadrant analysis of vertical turbulent scalar flux (Kutul et al. 1997).

Above the building array, turbulence coherent structures such as low- and high-speed flow structures are actually lifted and sunken parts of the interface ($u = 5.5 \text{ m s}^{-1}$) between the low- and high-speed air (Figs. 5a,d). Thus, low- and high-speed flow structures can be captured by just plotting the contours of equal streamwise velocity magnitude. The magnitude of 5.5 m s^{-1} is selected in this study (Park and Baik 2013). In both the NH and BH cases, low-speed streaks or streamwise elongated low-speed regions appear at $z/H = 3$ (stippled) and high-speed streaks appear at $z/H = 1.2$ (hatched). At $z/H = 3$, scalar ejections are concentrated on the low-speed regions in the NH and BH cases. Ejections of momentum occur successively (not shown), which induce streamwise elongated low-speed flow structures at $z/H = 3$ (Park and Baik 2013). On the other hand, scalar ejections tend to occur in a plume shape (not much streamwise elongated) in both the NH and BH cases. Especially in the BH case, scalar ejections following thermal updrafts appear at $z/H = 3$ between $y/H \sim 8$ and $y/H \sim 18$, showing more plumelike structures (Fig. 5e). It is also remarkable that one large secondary circular flow (stronger than that in the NH case) dominates the whole model domain with updrafts intensified by bottom heating in the BH case. Thus, the strengthened secondary circular flow induces streamwise elongated low-speed regions ($22 < y/H < 24$ and $0 < y/H < 3$), where scalar ejections occur frequently, and wide high-speed regions ($4 < y/H < 20$), where scalar ejections occur intermittently at $z/H = 3$. The low- and high-speed

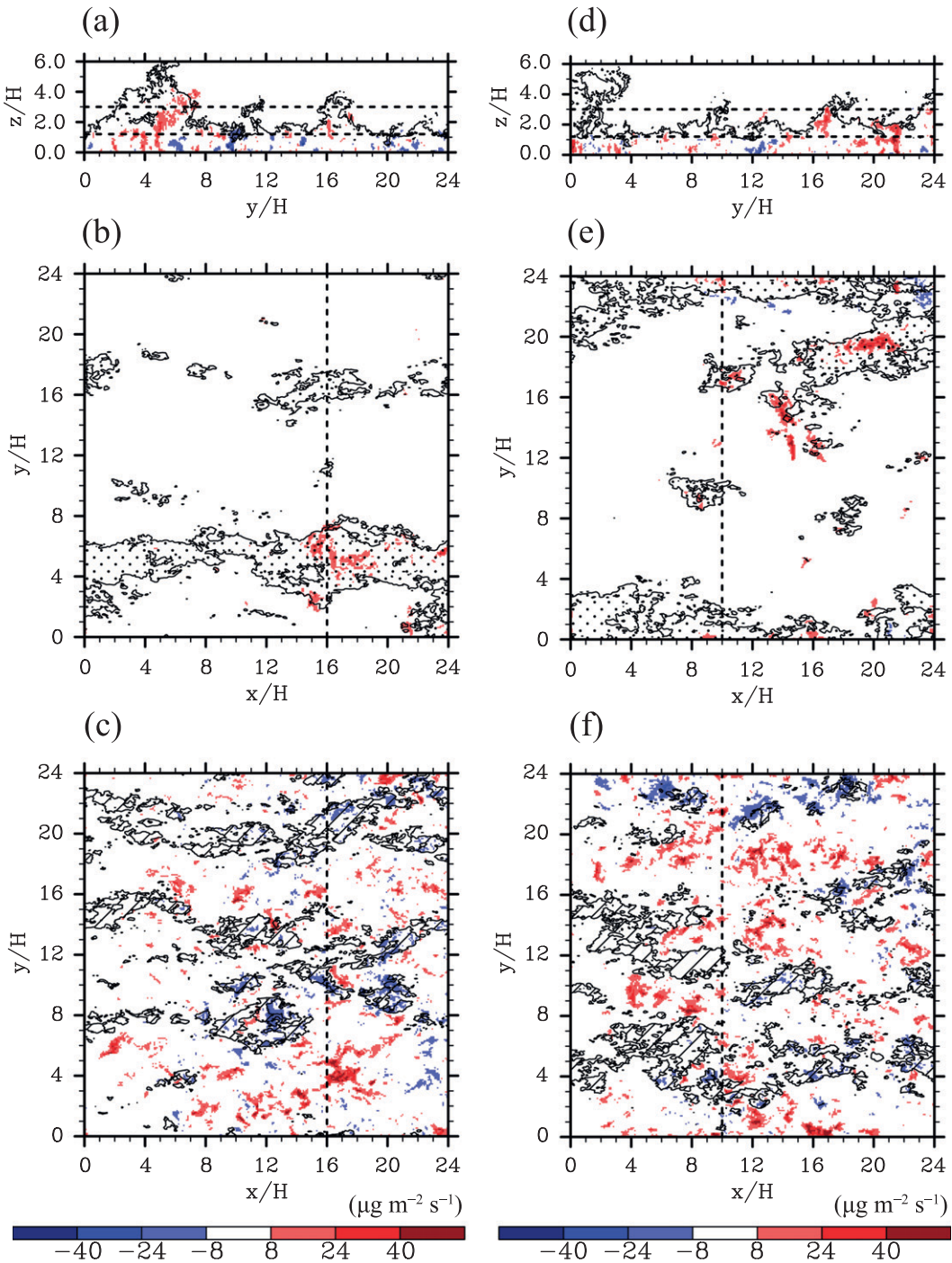


FIG. 5. Instantaneous fields of $\text{sgn}(w') \times \max(0, c'w')$ with the contours of equal streamwise velocity (5.5 m s^{-1}) at $t = 15480 \text{ s}$ in the (a) $y-z$ plane ($x/H = 16$), (b) $x-y$ plane ($z/H = 3$), and (c) $x-y$ plane ($z/H = 1.2$) in the NH case and those at $t = 19080 \text{ s}$ in the (d) $y-z$ plane ($x/H = 10$), (e) $x-y$ plane ($z/H = 3$), and (f) $x-y$ plane ($z/H = 1.2$) in the BH case. The stippled and hatched areas indicate low-speed regions at $z/H = 3$ and high-speed regions at $z/H = 1.2$, respectively.

regions are stable enough to be detected even in the time-averaged fields above $z/H \sim 2$ (not shown).

At $z/H = 1.2$, scalar transport events occur more frequently and both scalar ejection and scalar sweep

play an important role in transporting scalar upward (Figs. 5c,f). In both the NH and BH cases, scalar sweeps tend to appear in the high-speed regions and low scalar concentration air is entrained into the building array

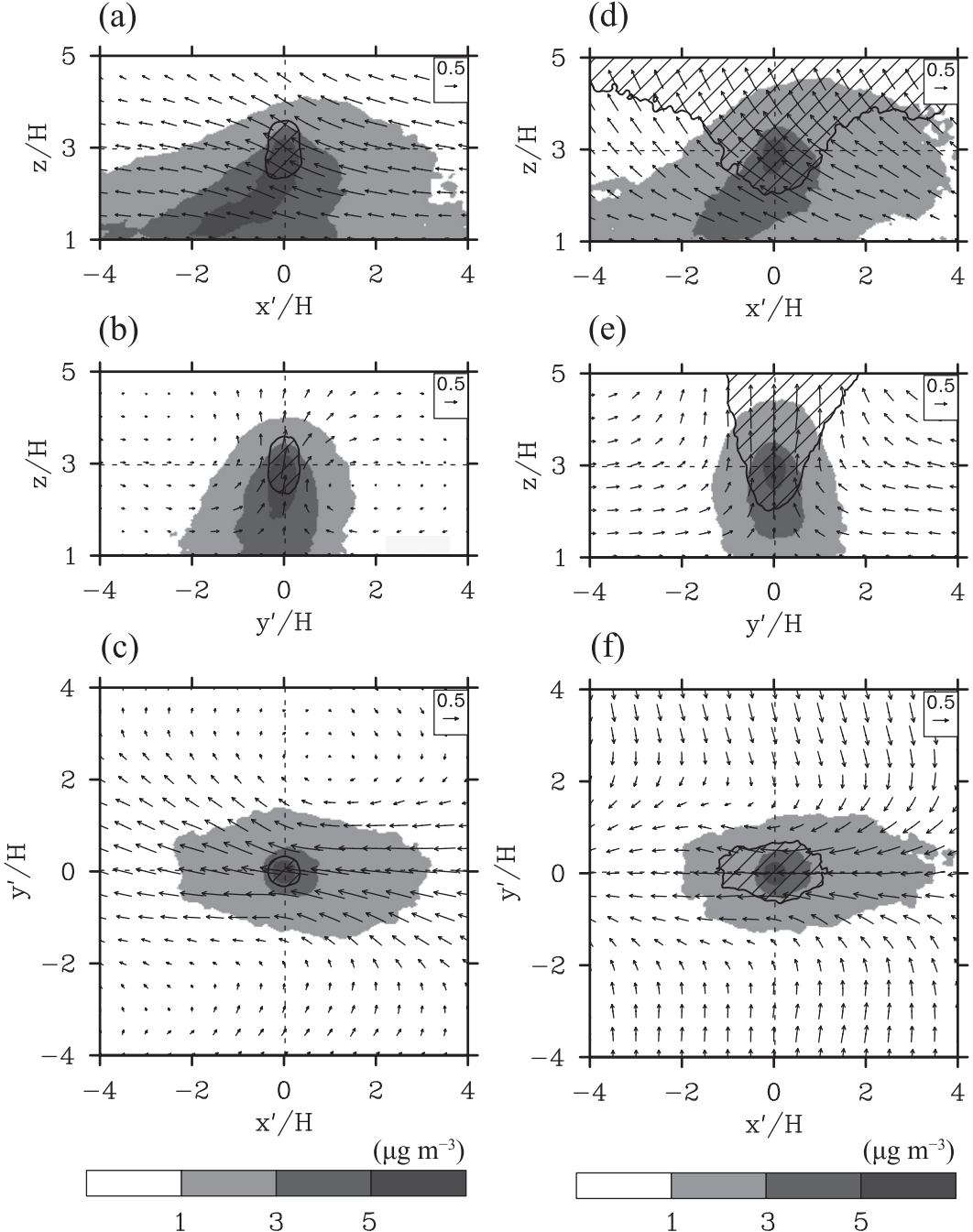


FIG. 6. Conditionally averaged c' and velocity vector fields in the (a),(d) x' - z plane ($y'/H = 0$), (b),(e) y' - z plane ($x'/H = 0$), and (c),(f) x' - y' plane ($z/H = 3$) in the (left) NH case and (right) BH case. Conditionally averaged u' instead of u is used for plotting velocity vector fields, and the contours of equal conditionally averaged vertical velocity (0.7 m s^{-1}) are added. The hatched areas indicate the regions where the conditionally averaged vertical velocity is higher than 0.7 m s^{-1} .

following scalar sweeps. Outside the high-speed regions, scalar ejections are dominant in the NH and BH cases.

Figure 6 shows conditionally averaged fields of scalar concentration perturbation and velocity vector fields with the contours of equal vertical velocity magnitude

(0.7 m s^{-1}). Conditional averages are obtained by sampling data around local maximum points where $c'w'$ is larger than $3.0 \mu\text{g m}^{-2}\text{s}^{-1}$. In both the NH and BH cases, plume structures of positive perturbations of scalar concentration are tilted downstream in the x' - z planes

and updrafts stronger than 0.7 m s^{-1} are located at the centers of perturbations. The combination of positive scalar concentration perturbation and updraft corresponds to scalar ejection, and this is the main scalar transport mechanism above the building array. Moreover, negative streamwise velocity perturbations coexist with updrafts in both the NH and BH cases (Fig. 6), implying that the momentum transport process and the scalar transport process are similar above the building array. Similar structures are detected in the NH and BH cases, but bottom heating induces stronger updrafts and stronger spanwise converging flow in the BH case (partially due to the large-scale secondary circular flow). Especially in the BH case, intensified updrafts appear in the streamwise elongated low-speed region and the low-speed region itself could be part of the large-scale secondary circular flow.

As shown in Fig. 5e, the patterns of scalar ejections are very different depending on the spanwise position at $z/H = 3$ in the BH case. To illustrate different patterns of scalar ejections, conditional averaging with additional criteria is conducted. First, the streamwise velocity perturbation from the horizontally averaged streamwise velocity at $z/H = 5$ is calculated. The region where the streamwise velocity perturbation is smaller than -0.5 m s^{-1} is defined as the upper low-speed region, and the region where the perturbation is larger than 0.2 m s^{-1} is defined as the upper high-speed region. These values are chosen to guarantee sufficient samples for different patterns of scalar ejections. Figure 7 shows conditionally averaged fields of scalar concentration perturbation and velocity vector fields with the contours of equal vertical velocity magnitude (0.7 m s^{-1}) below the upper low-speed regions and those below the upper high-speed regions in the BH case. Below the upper low-speed regions, scalar ejections develop well in the streamwise and vertical directions. In actuality, this kind of structure is part of the large-scale (covering the whole model domain) secondary circular flow and the secondary circular flow induces spanwise converging and diverging flow depending on the height. Even below the upper high-speed regions, bottom heating induces thermal updrafts and scalars are transported upward following the thermal updrafts. The thermal updrafts are not merged and not arranged in a line, however. Thus, the structure of the scalar ejections below the upper high-speed regions seems to be isolated and the vertical size of the scalar ejections is limited by the upper high-speed flow.

c. Scalar dispersion in a building array

To investigate thermal effects on overall scalar transport in the building array, mean and turbulent scalar fluxes summed over the windward, top, and leeward

surfaces of a virtual box in Fig. 1b ($11 \leq x/H \leq 13$, $0 \leq y/H \leq 24$, $0 \leq z/H \leq 1$) are calculated (Table 1). Rows in Table 1 indicate, in regular sequence, vertical scalar emission flux from the bottom surface, streamwise turbulent scalar flux at the windward surface, vertical turbulent scalar flux at the top surface, streamwise turbulent scalar flux at the leeward surface, streamwise mean scalar flux at the windward surface, vertical mean scalar flux at the top surface, streamwise mean scalar flux at the leeward surface, sum of all scalar fluxes, and the ratio of vertical turbulent scalar flux at the top surface to bottom scalar emission flux. The sign of the summed flux indicates the direction of the flux. Positive and negative fluxes indicate influx into the box and efflux from the box, respectively. The main sources of scalars in the box are scalar advection from upstream by streamwise mean flow and scalar emission from the bottom surface in both the NH and BH cases. Plenty of scalars in the box move downstream along the streamwise mean flow, and part of the scalars escape the box, following vertical turbulent motions at the top surface. In both the NH and BH cases, the magnitude of streamwise turbulent scalar flux summed over the windward or leeward surfaces is comparable in order to the magnitude of vertical turbulent scalar flux summed over the top surface. Owing to turbulent vertical motions strengthened by bottom heating, the ratio of the vertical turbulent scalar flux at the top surface to the scalar emission flux at the bottom surface in the BH case is larger than the ratio in the NH case.

To compare the net contribution of surface-summed scalar fluxes to the mean scalar budget in the virtual box, the rates of scalar amount coming into the box and escaping the box by turbulent scalar advection ($\Delta \bar{c}' u'$), mean scalar advection ($\Delta \bar{c} \bar{u}$), vertical turbulent scalar flux ($\bar{c}' w'_{z=H}$), and vertical mean scalar flux ($\bar{c} \bar{w}_{z=H}$) are plotted in Fig. 8. Streamwise mean scalar fluxes at the windward ($x/H = 11$) and leeward ($x/H = 13$) surfaces are large in magnitude (Table 1) but they balance each other, leading to net loss of scalar in the box. In the NH case, most of the scalar emission flux at the bottom surface is balanced by the mean streamwise scalar advection (the difference of streamwise mean scalar fluxes at the windward and leeward surfaces) and vertical turbulent scalar flux summed over the top surface. In the NH case, the vertical turbulent scalar flux is mainly composed of scalar ejection ($\bar{c}'_+ w'_{+z=H}$) and scalar sweep ($\bar{c}'_- w'_{-z=H}$), and the contributions (to the mean scalar budget in the virtual box) of the two scalar transport events are similar in magnitude. In comparison, in the BH case the vertical turbulent scalar flux summed over the top surface increases while the mean streamwise scalar advection decreases. This indicates that stronger vertical turbulent scalar transport decreases mean scalar

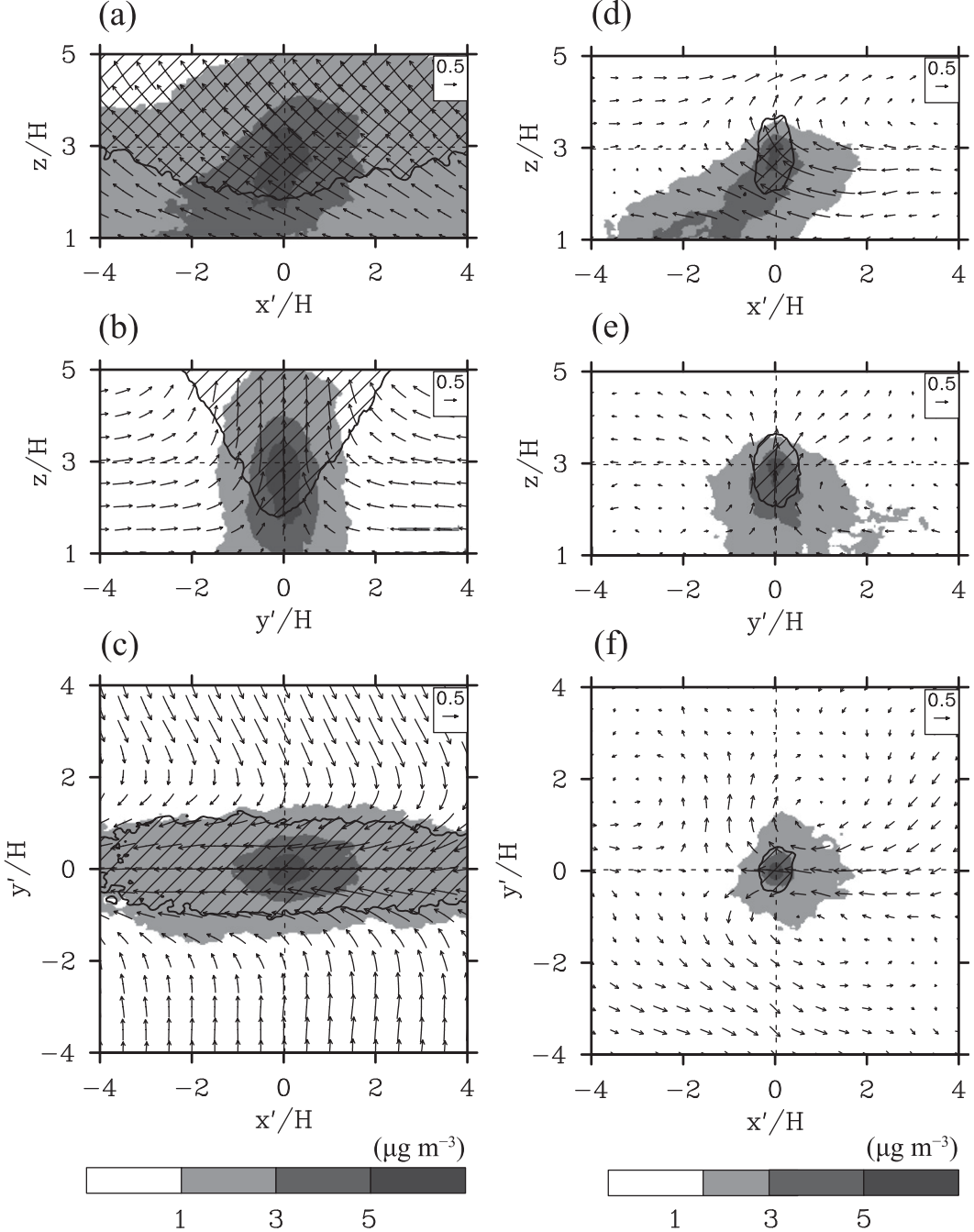


FIG. 7. As in Fig. 6, but (left) below upper low-speed regions and (right) below upper high-speed regions in the BH case.

concentration in the building array, reducing the amount of mean streamwise scalar advection. It is also noticeable that the contribution of scalar ejection is slightly larger than that of scalar sweep in the BH case.

Figure 9 shows time-averaged (for 1800 s) scalar concentration fields at $z/H = 0.1$ and the contours of equal streamwise velocity magnitude (6 m s^{-1}) at $z/H = 3$ in

the NH and BH cases. Because low-speed flow structures passing above the building array do not move much in the spanwise direction as they move downstream, low-speed flow structures can be seen as streamwise elongated low-speed regions in the time-averaged streamwise velocity fields. This kind of low-speed flow structure might be associated with the steady secondary circulation, as has

TABLE 1. Scalar fluxes ($\mu\text{g s}^{-1}$) summed over the three surfaces of the virtual box in the NH and BH cases. Overbars represent time averages.

	NH	BH
$\int_0^{24H} \int_{11H}^{13H} (\bar{c}'w')_{z=0} dx dy$	72 000	72 000
$\int_0^{24H} \int_0^H (\bar{c}'u')_{x=11H} dz dy$	-46 842	-31 059
$-\int_0^{24H} \int_{11H}^{13H} (\bar{c}'w')_{z=H} dx dy$	-51 385	-54 423
$-\int_0^{24H} \int_0^H (\bar{c}'u')_{x=13H} dz dy$	50 458	30 229
$\int_0^{24H} \int_0^H (\bar{c}u)_{x=11H} dz dy$	226 196	155 436
$-\int_0^{24H} \int_{11H}^{13H} (\bar{c}w)_{z=H} dx dy$	-4259	-5514
$-\int_0^{24H} \int_0^H (\bar{c}u)_{x=13H} dz dy$	-243 122	-164 425
Sum	3047	2244
$\int_0^{24H} \int_{11H}^{13H} (\bar{c}'w')_{z=H}/(\bar{c}'w')_{z=0} dx dy (\%)$	71.4	75.6

also been observed in wind-tunnel experiments (Reynolds et al. 2007). Below the low-speed region at $y/H \sim 5$, scalars converge following the spanwise converging flow (Fig. 6) in the NH case. In actuality, there exists another low-speed region at $y/H \sim 16$ in the NH case, and its existence can be confirmed by the weakly converging scalars. In the BH case, the scalar distribution pattern seems to be more dependent on the large-scale spanwise motion. The large-scale secondary circular flow, developing above the bottom-heated building array, induces

high scalar concentration below the rooftop height at $y/H \sim 23$. Scalar concentration fields at other heights ($z/H \sim 0.5$) have similar distribution patterns (high scalar concentration below low-speed regions) in both the NH and BH cases, confirming the dominant influence of flow structures above the building array on scalar dispersion in the building canopy layer. The large-scale secondary circular flow in the BH case is closely related to the roll structure in the atmospheric boundary layer flow. Because of the limited spanwise domain size of the simulation presented here, only one secondary circular flow structure is simulated in the BH case. Several secondary circular flow structures appear in an additional simulation with a larger horizontal model domain and a capping inversion (not shown), and their spanwise scale is about 2–3 times the inversion height (Kim and Park 2003).

As shown in Fig. 9, the scalar concentration in the building array is very dependent on flow structures above the building array. The effects of the flow structures above the building array on scalar fields in the building array can manifest across the interface that is usually located at the rooftop height. To examine characteristic scalar transport patterns, conditional averaging is done for the data sampled at local maximum points of instantaneous vertical turbulent scalar flux at the rooftop height. There are not any well-organized structures

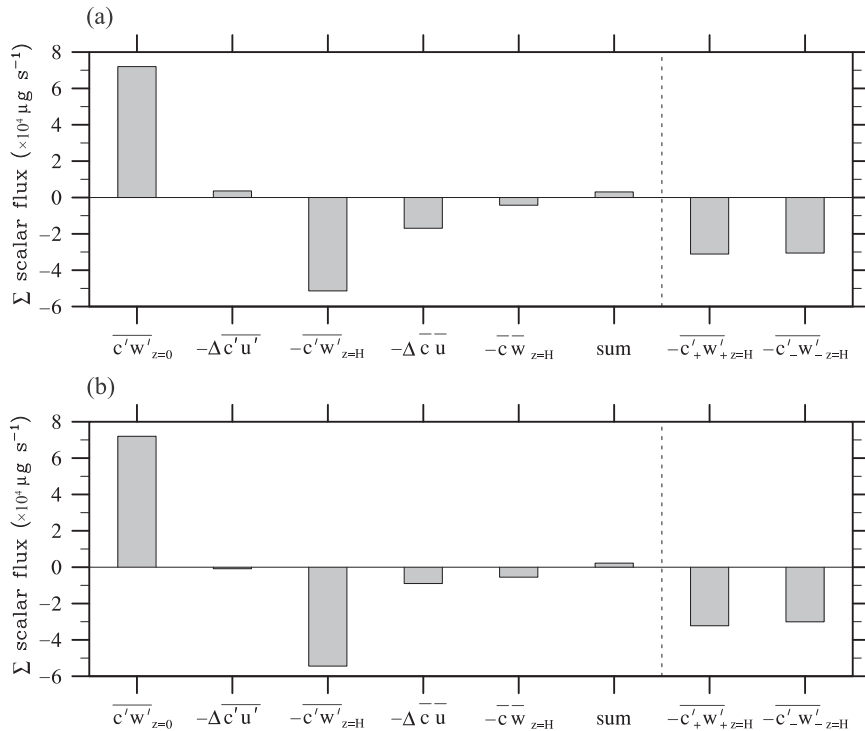


FIG. 8. Scalar fluxes summed over the surfaces of the virtual box (Fig. 1b) in the (a) NH and (b) BH cases. Positive and negative signs indicate influx into the box and efflux from the box, respectively.

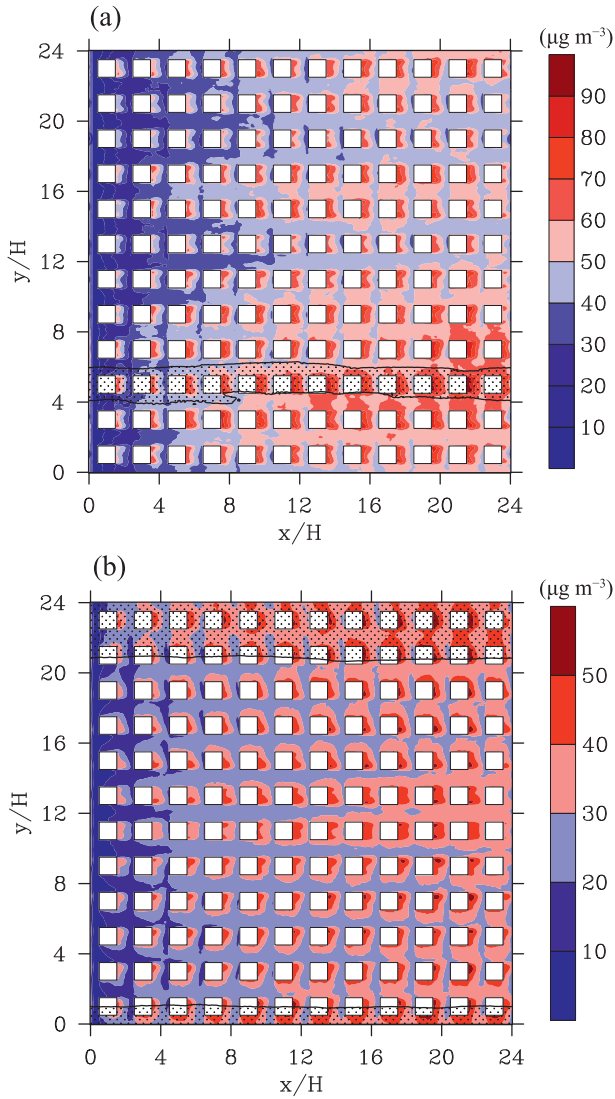


FIG. 9. Time-averaged scalar concentration fields at $z/H = 0.1$ and the contours of equal streamwise velocity magnitude (6 m s^{-1}) at $z/H = 3$ in the (a) NH and (b) BH cases. The stippled areas indicate the regions where the mean streamwise velocity is lower than 6 m s^{-1} at $z/H = 3$.

in the conditionally averaged fields (not shown), however, because two characteristic scalar transport events (scalar ejection and scalar sweep) are related to the flow structures in opposite vertical directions and they cancel each other out. Thus, the two kinds of events should be sampled separately to distinguish the two scalar transport patterns.

After applying additional criteria related to the sign of vertical velocity, two kinds of scalar transport patterns are obtained separately. Figure 10 shows scalar concentration perturbation and velocity vector fields conditionally averaged at $z/H = 1$ with the criteria $c'w' > 15 \mu\text{g m}^{-2} \text{s}^{-1}$ and $w > 0 \text{ m s}^{-1}$ and those with the differing

criteria $c'w' > 15 \mu\text{g m}^{-2} \text{s}^{-1}$ and $w < 0 \text{ m s}^{-1}$ in the NH case. In the NH case, scalar ejections occur with low-speed flow structures and scalar sweeps occur with high-speed flow structures. Scalar ejections seem to be well developed in the streamwise direction, and they tend to appear in the upstream part of the streamwise elongated low-speed flow structures (Fig. 10c). On the contrary, high-speed flow structures, occurring with scalar sweeps, tend to be compact in the streamwise direction. Low- and high-speed flow structures above the building array induce scalar ejections and scalar sweeps at the rooftop height, respectively. Furthermore, they induce converging and diverging spanwise flow in the building array, leading to spanwise variation of mean scalar concentration therein (Fig. 9). The streamwise scale of high-speed flow structures is smaller than that of low-speed flow structures because some of the high-speed flow structures are locally generated by shear instability at the tops of cavity spaces and the size of scalar sweeps is also limited by the building blocks. The limited size of scalar sweeps at the rooftop height is again related to the maximum of multiresolution cospectra of c and w at the short averaging width (8 s) over the CC points (Fig. 4c). In the BH case, similar structures (having a larger magnitude than those in the NH case) appear in the conditionally averaged fields.

Although scalar dispersion patterns in the streamwise and vertical directions are dominant above the building array, scalar dispersion patterns following spanwise turbulent motions are distinct in the building array. In the instantaneous spanwise scalar flux fields, spanwise elongated patterns through the cavity spaces appear (not shown). The traces of spanwise elongated scalar flux can be observed in the spanwise turbulent scalar flux fields.

Figure 11 shows spanwise turbulent scalar flux fields at $z/H = 0.1$ and the contours of equal streamwise velocity magnitude (6 m s^{-1}) at $z/H = 3$ in the NH and BH cases. To illustrate the position of high-speed regions, the contours of equal streamwise velocity magnitude (4.4 m s^{-1} in the NH case; 4.9 m s^{-1} in the BH case) at $z/H = 1.2$ are additionally plotted in Fig. 11. In the building array, positive and negative spanwise turbulent scalar fluxes appear mainly in and around the cavity spaces, and its sign tends to depend on the position of the low- and high-speed flow structures. As shown in Fig. 10, low- and high-speed flow structures above the building array induce spanwise converging and diverging flow in the building array, leading to spanwise channeling flow therein. It is also noticeable that scalar sweeps (and negative scalar concentration perturbations) become more dominant than scalar ejections as the height decreases in the building canopy layer in both the NH and BH cases (Fig. 3d). Thus, negative scalar concentration perturbations

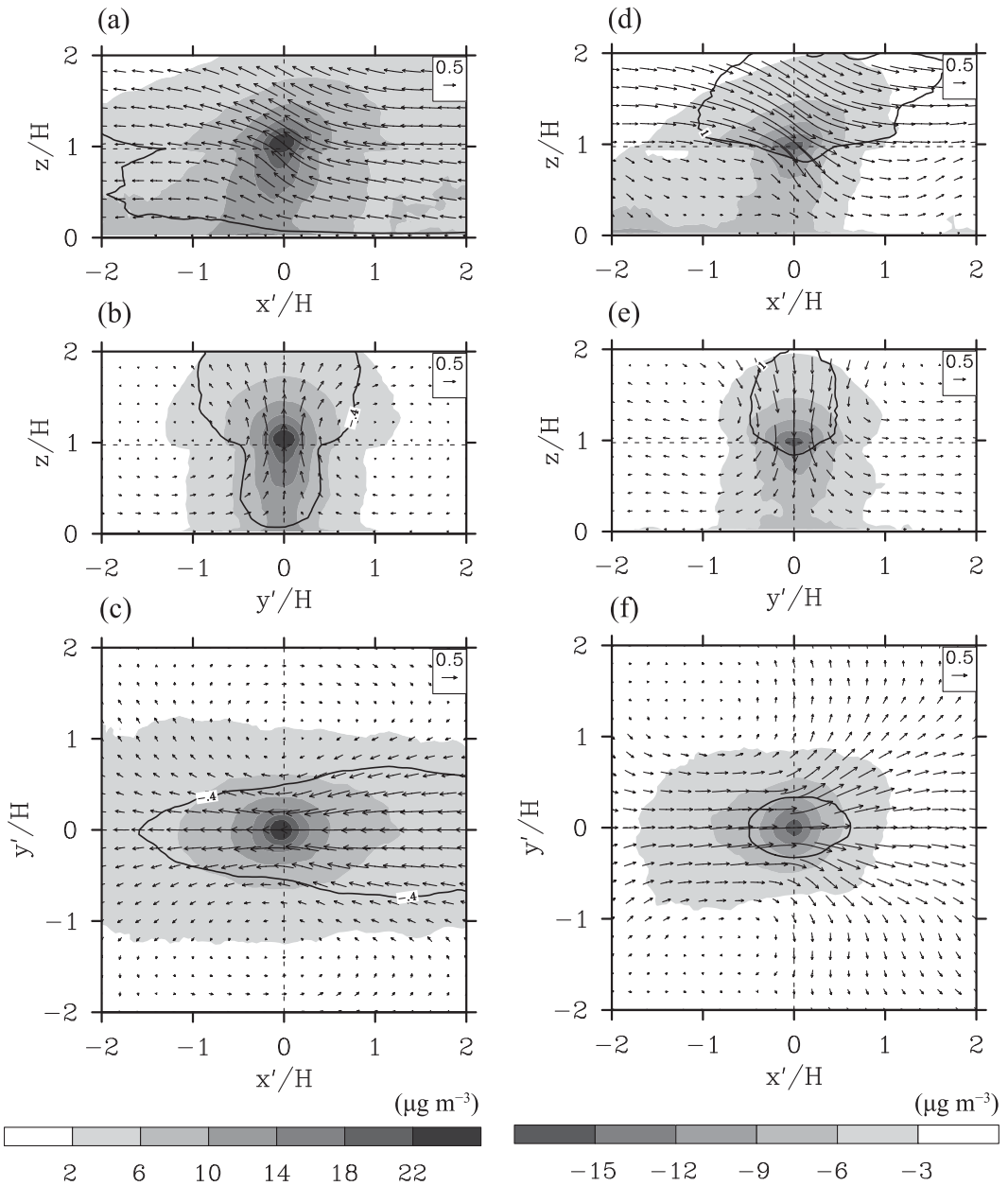


FIG. 10. Conditionally averaged c' and velocity vector fields in the (a),(d) x' - z plane ($y'/H = 0$), (b),(e) y' - z plane ($x'/H = 0$), and (c),(f) x' - y' plane ($z/H = 1$) for (left) scalar ejection and (right) scalar sweep in the NH case. Conditionally averaged u' instead of u is used for plotting velocity vector fields, and the contours of equal conditionally averaged streamwise velocity perturbation are added (-0.4 m s^{-1} for scalar ejection; 1 m s^{-1} for scalar sweep).

tend to induce positive spanwise turbulent scalar flux ($c' < 0$; $v' < 0$) and negative spanwise turbulent scalar flux ($c' < 0$; $v' > 0$) at the south and north of the high-speed regions in the NH and BH cases. Although instantaneous spanwise scalar flux fields show spanwise elongated structures (occupying the nearby intersection spaces), structures in the time-averaged spanwise

turbulent scalar flux fields seem to be confined in and around the cavity spaces because of the streamwise mean flow in the intersection spaces in both the NH and BH cases. The large-scale secondary circular flow in the BH case also affects turbulent spanwise scalar flux fields by inducing intermittent strong spanwise flow therein. Negative and positive spanwise turbulent scalar fluxes

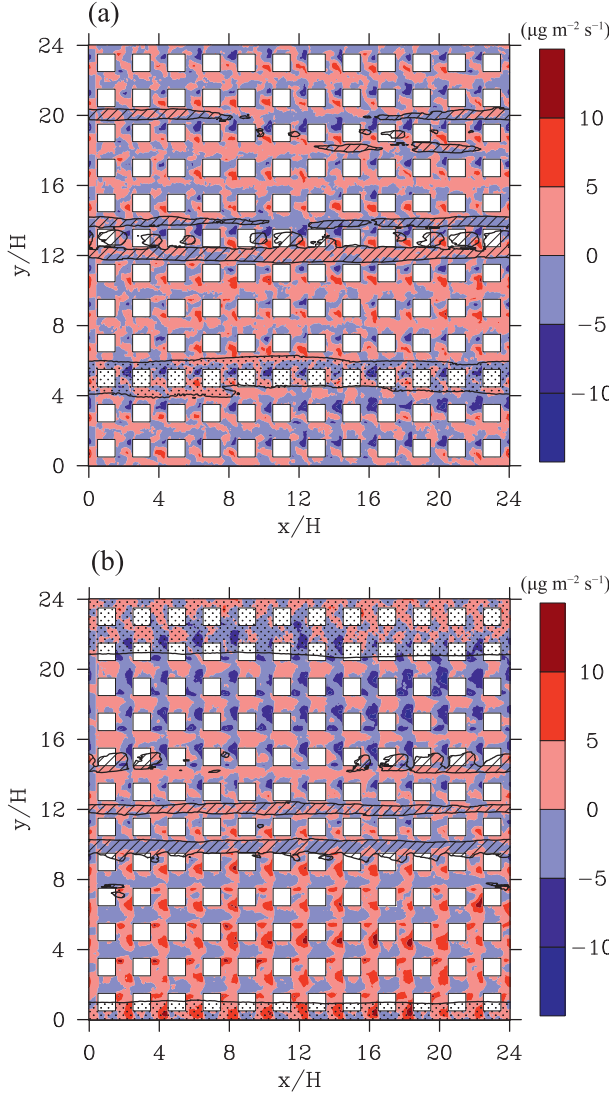


FIG. 11. Spanwise turbulent scalar flux fields at $z/H = 0.1$, the contours of equal streamwise velocity magnitude (6.0 m s^{-1}) at $z/H = 3$, and the contours of equal streamwise velocity magnitude (4.4 m s^{-1} in the NH case; 4.9 m s^{-1} in the BH case) at $z/H = 1.2$ in the (a) NH and (b) BH cases. The stippled and hatched areas indicate low-speed regions at $z/H = 3$ and high-speed regions at $z/H = 1.2$, respectively.

appear in the north and south of the high-speed flow structures, constantly transporting scalar toward the region below the low-speed flow structures in the BH case (Fig. 11b).

5. Summary and conclusions

Thermal effects on scalar dispersion in and above a cubical building array were investigated using an LES model. No-heating and bottom-heating cases were simulated and were compared with each other. Above the

building array, low- and high-speed flow structures appear and scalar ejections and scalar sweeps in the low- and high-speed flow structures, respectively, transport scalar upward in both the NH and BH cases. In the conditionally averaged fields at $z/H = 3$, the plume structure of positive scalar concentration perturbation appears with updrafts in the NH case, indicating the dominant role of scalar ejections in transporting scalar upward. In the BH case, a large-scale secondary circular flow is well developed as a result of intensified updrafts and the large-scale secondary circular flow is combined with the streamwise elongated low-speed regions above the building array. Applying additional criteria that are based on streamwise velocity magnitude at $z/H = 5$ in obtaining the conditional averaged fields at $z/H = 3$, streamwise elongated and isolated plume structures of scalar concentration perturbation are detected below the upper low-speed and upper high-speed regions, respectively.

Although scalar ejections are more important than scalar sweeps in vertical scalar transport at $z/H = 3$, the role of scalar sweeps in vertical scalar transport becomes important as the height approaches $z/H = 1$. Just above the rooftop height ($z/H = 1.2$), scalar sweeps in the high-speed regions appear with scalar ejections outside the high-speed regions and both the turbulent events transport scalar upward from the building array in the NH and BH cases. In the building array, the scalar emission flux at the bottom surface is mainly balanced by vertical turbulent scalar flux at the rooftop height and mean streamwise scalar advection. In comparison with the NH case, the magnitude of mean streamwise scalar advection decreases and the magnitude of vertical turbulent scalar flux increases in the BH case. The contribution (to the mean scalar budget) of scalar ejection is slightly larger than that of scalar sweep in the BH case whereas both contributions are similar in magnitude in the NH case.

Below the rooftop height, the distribution of time-averaged scalar concentration is dependent upon the turbulence coherent structures above the building array in both the NH and BH cases. The time-averaged scalar concentration is high and low below the low- and high-speed regions, respectively. In the NH case, positive and negative scalar concentration perturbations appear in the conditionally averaged fields at $z/H = 1$ depending on the sign of vertical velocity, and they correspond to scalar ejections and scalar sweeps, respectively. Scalar sweeps tend to appear with streamwise elongated low-speed flow structures while high-speed flow structures combined with scalar sweeps show compact shape in the horizontal plane at the rooftop height. In the BH case, bottom heating affects the magnitudes of the two scalar transport events. The low- and high-speed flow structures

at or above the rooftop height also induce spanwise converging and diverging turbulent flow in the building array, leading to spanwise turbulent scalar transport in both the NH and BH cases. Furthermore, the large-scale secondary circular flow in the BH case strengthens spanwise flow and spanwise scalar transport in the building array.

In densely built-up urban areas, variations in building geometry and heating intensity are important factors affecting turbulent flow and scalar dispersion therein. For example, buildings taller than surrounding buildings induce larger drag (Xie et al. 2008), and they also induce elevated scalar sources by inducing upward flow along their leeward walls (Pascheke et al. 2008). Further study is needed to investigate scalar dispersion with different building geometries and heating intensities.

Acknowledgments. The authors are grateful to three anonymous reviewers for providing valuable comments on this work. This work was supported by National Research Foundation of Korea (NRF) Grant 2012-0005674 funded by the Korea Ministry of Education, Science and Technology (MEST) and was also supported by the Brain Korea 21 Project (through the School of Earth and Environmental Sciences of Seoul National University).

REFERENCES

- Coceal, O., A. Dobre, and T. G. Thomas, 2007: Unsteady dynamics and organized structures from DNS over an idealized building canopy. *Int. J. Climatol.*, **27**, 1943–1953.
- Davidson, M. J., K. R. Mylne, C. D. Jones, J. C. Phillips, R. J. Perkins, J. C. H. Fung, and J. C. R. Hunt, 1995: Plume dispersion through large groups of obstacles—A field investigation. *Atmos. Environ.*, **29**, 3245–3256.
- Deardorff, J. W., 1980: Stratocumulus-capped mixed layers derived from a three-dimensional model. *Bound.-Layer Meteor.*, **18**, 495–527.
- Howell, J. F., and L. Mahrt, 1997: Multiresolution flux decomposition. *Bound.-Layer Meteor.*, **83**, 117–137.
- Kanda, M., R. Moriwaki, and F. Kasamatsu, 2004: Large-eddy simulation of turbulent organized structures within and above explicitly resolved cube arrays. *Bound.-Layer Meteor.*, **112**, 343–368.
- Katul, G., G. Kuhn, J. Schieldge, and C.-I. Hsieh, 1997: The ejection-sweep character of scalar fluxes in the unstable surface layer. *Bound.-Layer Meteor.*, **83**, 1–26.
- Kim, J.-J., and J.-J. Baik, 1999: A numerical study of thermal effects on flow and pollutant dispersion in urban street canyons. *J. Appl. Meteor.*, **38**, 1249–1261.
- , and —, 2004: A numerical study of the effects of ambient wind direction on flow and dispersion in urban street canyons using the RNG $k-\epsilon$ turbulence model. *Atmos. Environ.*, **38**, 3039–3048.
- Kim, S.-W., and S.-U. Park, 2003: Coherent structures near the surface in a strongly sheared convective boundary layer generated by large-eddy simulation. *Bound.-Layer Meteor.*, **106**, 35–60.
- Letzel, M. O., M. Krane, and S. Raasch, 2008: High resolution urban large-eddy simulation studies from street canyon to neighbourhood scale. *Atmos. Environ.*, **42**, 8770–8784.
- Louka, P., G. Vachon, J.-F. Sini, P. G. Mestayer, and J.-M. Rosant, 2002: Thermal effects on the airflow in a street canyon—Nantes'99 experimental results and model simulations. *Water Air Soil Pollut. Focus*, **2**, 351–364.
- Macdonald, R. W., R. F. Griffiths, and S. C. Cheah, 1997: Field experiments of dispersion through regular arrays of cubic structures. *Atmos. Environ.*, **31**, 783–795.
- Mahrt, L., and W. Gibson, 1992: Flux decomposition into coherent structures. *Bound.-Layer Meteor.*, **60**, 143–168.
- Meroney, R. N., M. Pavageau, S. Rafailidis, and M. Schatzmann, 1996: Study of line source characteristics for 2-D physical modeling of pollutant dispersion in street canyon. *J. Wind Eng. Ind. Aerodyn.*, **62**, 37–56.
- Michioka, T., A. Sato, H. Takimoto, and M. Kanda, 2011: Large-eddy simulation for the mechanism of pollutant removal from a two-dimensional street canyon. *Bound.-Layer Meteor.*, **138**, 195–213.
- Moeng, C.-H., and P. P. Sullivan, 1994: A comparison of shear- and buoyancy-driven planetary boundary layer flows. *J. Atmos. Sci.*, **51**, 999–1022.
- Park, S.-B., and J.-J. Baik, 2013: A large-eddy simulation study of thermal effects on turbulence coherent structures in and above a building array. *J. Appl. Meteor. Climatol.*, **52**, 1348–1365.
- , —, S. Raasch, and M. O. Letzel, 2012: A large-eddy simulation study of thermal effects on turbulent flow and dispersion in and above a street canyon. *J. Appl. Meteor. Climatol.*, **51**, 829–841.
- Pascheke, F., J. F. Barlow, and A. Robins, 2008: Wind-tunnel modeling of dispersion from a scalar area source in urban-like roughness. *Bound.-Layer Meteor.*, **126**, 103–124.
- Piacsek, S. A., and G. P. Williams, 1970: Conservation properties of convection difference schemes. *J. Comput. Phys.*, **6**, 392–405.
- Raasch, S., and M. Schröter, 2001: PALM—A large-eddy simulation model performing on massively parallel computers. *Meteor. Z.*, **10**, 363–372.
- Reynolds, R. T., P. Hayden, I. P. Castro, and A. G. Robins, 2007: Spanwise variations in nominally two-dimensional rough-wall boundary layers. *Exp. Fluids*, **42**, 311–320.
- Sini, J.-F., S. Anquetin, and P. G. Mestayer, 1996: Pollutant dispersion and thermal effects in urban street canyons. *Atmos. Environ.*, **30**, 2659–2677.
- Takimoto, H., A. Sato, J. F. Barlow, R. Moriwaki, A. Inagaki, S. Onomura, and M. Kanda, 2011: Particle image velocimetry measurements of turbulent flow within outdoor and indoor urban scale models and flushing motions in urban canopy layers. *Bound.-Layer Meteor.*, **140**, 295–314.
- Uehara, K., S. Murakami, S. Oikawa, and S. Wakamatsu, 2000: Wind tunnel experiments on how thermal stratification affects flow in and above urban street canyons. *Atmos. Environ.*, **34**, 1553–1562.
- Walton, A., and A. Y. S. Cheng, 2002: Large-eddy simulation of pollution dispersion in an urban street canyon—Part II: Idealised canyon simulation. *Atmos. Environ.*, **36**, 3615–3627.
- Xie, Z.-T., O. Coceal, and I. P. Castro, 2008: Large-eddy simulation of flows over random urban-like obstacles. *Bound.-Layer Meteor.*, **129**, 1–23.